

1
2 Effects of Retained Austenite Volume Fraction, Morphology, and
3 Carbon Content on Strength and Ductility of Nanostructured
4 TRIP-assisted Steels

5
6 Y.F. Shen ^{a,*}, L.N. Qiu ^a, X. Sun ^b, L. Zuo ^a, P.K. Liaw ^c, and D. Raabe ^{d,*}

7
8 ^aKey Laboratory for Anisotropy and Texture of Materials (MOE), Northeastern University, Shenyang 110004,
9 China

10 ^bPacific Northwest National Laboratory, PO Box 999, Richland, WA 99352, USA

11 ^cDepartment of Materials Science and Engineering, The University of Tennessee, Knoxville, TN 37996, USA

12 ^dMax-Planck-Institut fuer Eisenforschung Max-Planck-Str. 1, 8 40237 Düsseldorf, Germany

13
14 Submitted to: **Materials Science & Engineering A**

15 April, 2015

16
17 (with 12 figures)

18
19
20 *Corresponding author

21 Y.F. Shen

22
23 Key Laboratory for Anisotropy and Texture of Materials (MOE), Northeastern
24 University, 3 Wenhua Road, Shenyang 110004, P.R. China

25 Phone: +86-24-8368-1455(office)

26 Fax: +86-24-2390-6472

27 E-mail: shenyf@smm.neu.edu.cn

1 **Abstract:** With a suite of multi-modal and multi-scale characterization techniques,
2 the present study unambiguously proves that a substantially-improved combination of
3 ultrahigh strength and good ductility can be achieved by tailoring the volume fraction,
4 morphology, and carbon content of the retained austenite (RA) in a
5 transformation-induced-plasticity (TRIP) steel with the nominal chemical
6 composition of 0.19C-0.30Si-1.76Mn-1.52Al (weight percent, wt.%). After
7 intercritical annealing and bainitic holding, a combination ultimate tensile strength
8 (UTS) of 1,100 MPa and true strain of 50% has been obtained, as a result of the
9 ultrafine RA lamellae, which are alternately arranged in the bainitic ferrite around
10 junction regions of ferrite grains. For reference, specimens with a blocky RA,
11 prepared without the bainitic holding, yield a low ductility (35%) and a low UTS (800
12 MPa). The volume fraction, morphology, and carbon content of RA have been
13 characterized using various techniques, including magnetic probing, scanning electron
14 microscopy (SEM), electron-backscatter-diffraction (EBSD), and transmission
15 electron microscopy (TEM). Interrupted tensile tests, mapped using EBSD in
16 conjunction with the kernel average misorientation (KAM) analysis, reveal that the
17 lamellar RA is the governing microstructure component responsible for the higher
18 mechanical stability, compared to the blocky one. By coupling these various
19 techniques, we quantitatively demonstrate that in addition to the RA volume fraction,
20 its morphology and carbon content are equally important in optimizing the strength
21 and ductility of TRIP-assisted steels.

22

23 **Keywords:** Retained austenite; morphology; mechanical stability; strength; ductility.

1. Introduction

Materials with good strength and excellent ductility are of paramount relevance for lightweight vehicles. In this context, transformation-induced-plasticity (TRIP) aided steels enable an excellent combination of strength and ductility, allowing substantial weight reduction without compromising safety standards. The properties of these steels are closely related to both the multiphase characteristics of their microstructures and the TRIP effect, *i.e.*, the martensitic transformation of the retained austenite (RA) induced by deformation [1-7]. The martensitic transformation and the associated accommodation plasticity lead to an increased strain-hardening, effectively delaying softening through premature strain localization [3-8]. This trend means that an increase in the work-hardening ability of the microstructural constituents can postpone the onset of necking and, thus, lead to a higher uniform elongation. Therefore, the TRIP effect improves the formability and energy absorption of such steels. Since the volume fraction and distribution of RA plays a key role in improving the mechanical properties of TRIP steels [9], the characterization and understanding of RA is important [8].

The TRIP-assisted multiphase steels typically contain an intercritical body-centered cubic (bcc) ferrite matrix, island-type metastable face-centered cubic (fcc) RA dispersed in the ferrite matrix, and a bainitic structure where ultrafine RA lamellae are embedded in the martensite [10]. The martensite is generally body-centered tetragonal (bct) or hexagonal-close-packed (hcp), depending on the carbon content [11, 12]. Good ductility results from the soft and ductile ferrite as well as from the TRIP effect, while the high strength originates from the bainite and the freshly-formed martensite induced by the martensitic transformation of the metastable RA [1-3, 13, 14]. Several reports [15-17] revealed that the volume fraction and

1 stability of RA at room temperature are essential factors in designing TRIP steels.
2 They are controlled mainly by the alloy composition, elemental partitioning, austenite
3 grain size, intercritical annealing temperature, and possible effects associated with
4 austenite reversion [4, 18-22]. In order to obtain a microstructure with a specific
5 amount and stability of RA, quenching and partitioning (Q&P) treatments [13, 17]
6 have proven to be effective in producing high-strength steels with a mixed
7 microstructure of the desired constituents [13, 18, 23-25]. The Q&P process suggested
8 by Speer and Matlock [18] includes quenching to a region between M_s and M_f
9 (martensite start-finish temperatures) and the partitioning at that temperature or a
10 higher temperature. The obtained microstructure is characterized by the
11 carbon-depleted martensite and carbon-enriched austenite. The intercritical annealing
12 temperature may control the RA volume fraction directly but not all of the RA
13 stability parameters mentioned above [16]. While all these factors play a role for the
14 properties of the low-alloy TRIP steels, it was reported that the influence of the
15 austenite fraction and its carbon concentration are particularly important [16].
16 However, in the open literature, few studies examined the effects of RA morphology
17 in conjunction with the above two factors on the overall strength and ductility of this
18 class of materials [26, 27].

19 The Q&P process generally does not involve a bainitic-holding step due to
20 the fact that bainite would normally not form below M_s [18]. During the Q&P
21 treatment, carbon partitioning takes place at a temperature higher than the quench
22 temperature to accelerate carbon diffusion from the martensite into the austenite [16,
23 18, 28]. Petrov et al. investigated the microstructure and texture of the
24 lightly-deformed TRIP steel by means of the electron-backscatter-diffraction (EBSD)
25 technique [29, 30]. The steel was subjected to intercritical annealing, followed by an

1 interrupted isothermal-quenching treatment in the low bainite region to obtain the
2 final microstructure. Their results have shown that the bcc phase accumulates the
3 main portion of the deformation, whereas the RA grains remain largely undeformed
4 with selective regions transformed into martensite. Grajcar and co-workers
5 characterized the microstructures of the thermomechanically-processed Si-Al TRIP
6 steel by X-ray diffraction (XRD) and EBSD [31]. Their results revealed that RA is
7 present as uniformly-distributed blocky grains in a ferritic matrix or thin layers
8 located between bainitic ferrite laths.

9 In a previous study [26], a commercial cold-rolled TRIP-assisted steel with a
10 chemical composition of 0.19C-0.30Si-1.76Mn-1.52Al (weight percent, wt.%) was
11 investigated, using intercritical annealing and subsequently bainitic holding to
12 promote the formation of bainitic ferrite (BF) above the martensite-start temperature.
13 The study confirmed that the intercritical annealing and bainitic holding can
14 effectively improve the mechanical properties for this steel by facilitating the
15 formation of RA and BF. Up till now, however, there is no systematic study on the
16 optimal heat-treatment parameters and their impact on the volume fraction,
17 morphology, and carbon content of the RA, and the resulting strength and ductility of
18 the steels. This situation is partly due to the large amount of experimental and
19 characterization work required at different lengths scales. Another reason lies in the
20 fact that different characterization methods typically lead to variations in the RA
21 volume-fraction measurements. In addition, some of the RA lath features in the
22 microstructures are so thin, extending into the nanoscopic regime, that only
23 transmission electron microscopy (TEM) can reveal the lath thickness and inter-lath
24 spacing in sufficient detail [32].

25 Here, we systematically examine the effects of heat-treatment parameters on

1 the RA volume fraction, morphology, and carbon concentration of a
2 commercially-available TRIP steel, and on their subsequent influence on the strength
3 and ductility of this class of multiphase steels. More specifically, this study uses a
4 multi-modal multi-scale experimental approach including XRD, magnetic
5 measurement, optical microscopy (OM), scanning-electron microscopy (SEM), EBSD,
6 and TEM in an attempt to quantitatively demonstrate that the RA volume fraction,
7 morphology, and carbon concentration are concurrent parameters influencing the
8 mechanical stability of RA in the deformation process, hence leading to different
9 ultimate strength and ductility of the TRIP-assisted steels. Based on the obtained
10 results, a microstructure-design strategy will be provided for further improving the
11 strength and ductility of this class of materials.

12

13 **2. Description of Experimental Methods**

14 **2.1. Heat treatments**

15 A commercial cold-rolled TRIP steel is used in this study. The alloying
16 elements are (in weight percent, wt.%): C 0.19, Si 0.30, Mn 1.76, Al 1.52, Ni 0.007,
17 Cu 0.007, Ti 0.002, Mo 0.003, P 0.012, N 0.003, S 0.004, balanced with Fe. The
18 initial microstructure consists of lath ferrite. The isothermal intercritical annealing
19 tests were performed, using a continuous annealing machine (CAS30011,
20 Northeastern University, China). To determine the temperature of austenization,
21 cylindrical samples with a diameter of 3 mm, and length of 10 mm were used to
22 conduct studies with a push-rod L78-RITA dilatometer (Linseis Messgeraete,
23 Germany). The sample temperature was measured by a thermocouple welded to the
24 surface using a precision welder and the jig supplied by the dilatometer manufacturer.
25 The heating and austenitization treatments were carried out in a vacuum of 5×10^{-8}

1 MPa, and the cooling process was achieved using argon gas. The specimen was
2 heated to 1,200°C with a heating rate of 10°C/s and kept at a temperature of 1,200°C
3 for 60s. A preliminary dilatometry study shows that the austenite-starting temperature
4 (A_{c1}) and austenite-finishing temperature (A_{c3}) are 712°C and 892°C for the
5 investigated steel, respectively, with an error within $\pm 2^\circ\text{C}$ [26]. Using various cooling
6 rates from 0.5 °C/s to 150 °C/s, the measured phase-transformation diagram for the
7 studied steel indicates (Fig. 1a) that the bainite-start temperature (B_s) and
8 bainite-finish (B_f) temperature are 450°C and 380°C, respectively, at a cooling rate of
9 40°C/s.

10 Seven steels, hereafter referred to as A, B, C, D, E, F, and G, were developed
11 by controlling the annealing temperature and the subsequent bainitic-holding
12 processes. First, the samples were annealed at a temperature of 750, 800, 820, 850,
13 and 880°C for 120s, respectively. After that, the specimen was quenched to a
14 temperature slightly above the martensite-start temperature (368°C) at a cooling rate
15 of 80°C/s. In order to promote the carbon partition into the austenite, subsequent
16 isothermal bainitic-holding treatments were carried out in a salt-bath furnace in the
17 bainite region of 400 – 450°C for 300 s prior to air cooling to room temperature (RT),
18 (Fig. 1b). As the baseline for comparison, steel H was obtained by annealing the
19 sample at 850°C for 120s and cooling to RT directly (Fig. 1c). Hereafter, the
20 TRIP-assisted steels are designated as steels A–H alphabetically with the following
21 heat-treatment parameters: A: 750°C/120s + 400°C/300s; B: 800°C/120s +
22 400°C/300s; C: 820°C/120s + 400°C/300s; D: 850°C/120s + 400°C/300s; E:
23 880°C/120s + 400°C/300s; F: 850°C/120s + 420°C/300s; G: 850°C/120s + 450°C/300s;
24 H: 850°C/120s.

25 It should be noted that an austenitization thermal treatment above A_{c3} will

yield a fully martensitic microstructure before the bainitic holding, which in principle should improve the microstructure homogeneity of the material. However, we only focus on the intercritical annealing treatment in this study with relatively low annealing temperatures to explore the possibility of optimizing properties while minimizing the production cost of future commercialization.

2.2. Mechanical behavior

To examine the effects of different heat treatments on the mechanical properties of the steels, the as-heat treated sheets were cut into dog-bone-shaped specimens with a gauge length of 20 mm and a width of 6 mm, and the final thickness of 1.2 mm after polishing. Uniaxial tensile tests were performed on a micro-force testing system (MTS, China CO., LTD.) at a constant strain rate of $5 \times 10^{-3} \text{s}^{-1}$ at RT. The tensile axis was parallel to the rolling direction. Some tests were interrupted at pre-defined deformation levels to study the RA content and the deformed microstructures as a function of true strain. For each condition, three tests were performed to obtain the average values of the mechanical properties.

2.3. Microstructural characterizations

2.3.1. Optical microscopy observations

An optical micrograph was performed, using the OLYMPUS GX71 optical microscope to examine the effect of heat treatment on the transformation processes in the steel. The specimens were cut from the central part of the heat-treated steel along the rolling direction (RD) using electrical-discharge machining. Subsequently, the specimens were mechanically polished using silica papers with gradually decreasing roughness. Finally, specimens were etched in a solution consisting of 9g sodium

hyposulfite and 3g carbazotic acid diluted with 90ml ethanol and 100ml deionized water for 20 – 30s. The etched samples were washed, using C₂H₅OH and then quickly dried with a hair dryer.

2.3.2. X-ray diffraction

Specimens were cut from the heat-treated sheet to determine the RA volume fraction, using the XRD, magnetic measurement, and EBSD analysis. Samples for the XRD analysis were chemically cleaned, using a mixture of 70 volume percent (vol. %) HCl and 30 vol. % HNO₃. The XRD measurement was performed on an X' Pert PRO diffractometer (PW3040/60, Panalytical B.V., Netherlands) equipped with a sample stage for the CoK α 1 anode (wavelength $\lambda = 0.1789$ nm) and an X-ray detector. Samples were scanned at a step size of 0.02° per second in the 2θ range from 40 to 80°. The penetration depth of the X-rays (CoK α 1 radiation) in steels is a few micrometers. For reducing surface effects and textures, the samples were chemically polished during the preparation and rotated during the XRD measurements. The raw data were background filtered. The volume fraction of the RA phase (V_γ) was determined by the integrated intensity of the (200) $_\gamma$, (220) $_\gamma$, and (311) $_\gamma$ austenite peaks and of the (200) $_\alpha$ and (220) $_\alpha$ ferrite peaks using the method described in references [26, 33-35].

2.3.3. Magnetic measurements

Magnetic measurements allow probing bulk materials [36]. Here, magnetic measurements were conducted to obtain the volume fraction of RA, using a vibration sample magnetometer (VSM) (Model 7047, Lakeshore, USA). The underlying rationale is that the RA phase is paramagnetic, while the ferrite, martensite, and cementite are ferromagnetic below the Curie point, T_C (210 and 770 °C for the cementite and pure ferrite, respectively) [37]. In the presence of the applied magnetic field, the relationship between the measured magnetization of the sample and the

1 applied magnetic field is obtained, and the saturation portion of the magnetization plot
2 is used for the determination of the volume fraction of RA. For the measurement of
3 the sheet sample with a dimension of $3 \times 3 \times 1 \text{ mm}^3$ in this study, the magnetic field
4 was applied to a maximum value of 2T and then decreased stepwise to 0T at RT.

5 2.3.4. SEM and EBSD analyses

6 The microstructure was characterized using SEM (FEI Quanta 600, PHILIPS,
7 USA) operated at a voltage of 20 kV. The EBSD measurements were carried out in a
8 plane perpendicular to the transverse direction of the sheet. The specimens for the
9 EBSD analyses were electro-polished for ~ 20s at an operating voltage of 20 V to
10 remove the damage of the surface caused by grinding and mechanical polishing. The
11 electrolyte consists of the 10 vol.% perchloric acid, 80 vol.% ethanol, and 10 vol.%
12 deionized water. EBSD analysis was conducted at an acceleration voltage of 20 kV,
13 sample tilt angle of 70° , and working distance of 7 mm. To obtain a representative
14 value for the respective phase fractions, it is important that the EBSD data cover a
15 large area and includes enough points at sufficiently small resolution. Hence, an area
16 of $1.0 \times 1.0 \text{ mm}^2$ was covered per specimen. Maps were measured on a hexagonal
17 grid with a step size of 0.1 μm . The EBSD data was collected on a SU-70 Hitachi
18 field-emission SEM and evaluated by the orientation-imaging-microscopy (OIM)
19 software. Grain confidence index standardization is used to identify small-angle
20 (between 2 and 15°) and large-angle grain boundaries ($> 15^\circ$). Grain boundaries with
21 an orientation difference below 2° were excluded, and values above this threshold
22 were counted as adjacent grains. The kernel average misorientation (KAM) function,
23 which is retrieved from the EBSD data, was employed in order to observe orientation
24 changes caused by plastic deformation. The KAM maps were progressively obtained
25 at the same location for steel C at different strain levels by analyzing the

corresponding EBSD maps with the TSLOIM software (up to the 5th neighbor shell and a maximum angle of 5°). This technique allows mapping the strain-distribution change at the same area during the entire deformation process.

2.3.5. TEM observations

TEM was used to study the microstructural changes associated with various heat-treatment processes. Specimens for the TEM observation were cut from the annealed samples and the homogeneously-deformed regions from the samples after tension, mechanically polished from both sides to a final thickness of about 50 µm. Subsequently, the foils were cut to a diameter of 3 mm and thinned using a double-jet electrolytic polisher at a voltage of 32 V and a temperature between - 10 and - 5°C. The composition of the electrolyte consisted of 10 vol.% perchloric acid and 90 vol.% ethanol. The TEM observations of strained samples were performed in a field-emission-gun (FEG) Tecnai G2 20 microscope, operating at an accelerated voltage of 200 kV.

3. Results and Discussion

3.1. Relationship between heat treatment parameters and RA characteristics

Figure 2 shows the optical micrographs of the samples after different heat treatments. For the identification of RA, the samples were etched by a chemical solution, as described in Section 2.3.1. Thus, the optical micrographs show different phases in different colors: ferrite in watchet, bainite in mazarine, and RA in brown/dark brown, respectively (Fig. 2). Similar observations were reported by Angeli, et al. [38]. Their investigations supported that the etching color mainly depends on the local carbon content, resulting from different chemical potentials of the individual phases. The ferrite and retained austenite-martensite are straightforward

1 to distinguish. The bainite constituents can essentially be determined by their
2 positions in the neighborhood of the austenite. Results from two different groups [19,
3 39, 40] suggest that the dark areas correspond to the austenite phase or to bainite
4 regions.

5 With annealing at the lowest temperature of 750°C for 120 s and bainitic
6 holding at 400°C for 300 s, the microstructure of steel A consists predominantly of
7 ferrite. The ferrite has an average grain size of ~ 10 μm and exhibits a strip-like
8 characteristic resulting from cold rolling. A few small granular RA are distributed
9 around the ferrite (Fig. 2a).

10 With increase in the annealing temperature, both the volume fraction and
11 morphology of the RA and bainite phases are changing. To further examine the
12 specific characteristics of the RA and bainite in the samples obtained from different
13 heat-treatment processes, closer observations were performed using SEM. The SEM
14 results in Fig. 3 for the differently heat-treated steels show consistent morphology
15 features, as compared to those shown in Fig. 2, while revealing more
16 microstructural-level details: with increasing the intercritical-annealing temperature,
17 the ferrite transforms from strip-like (Fig. 3a) to equiaxed microstructures (Figs.
18 3b-3h), with an average grain size of ~ 10μm. Steels B–G, processed with a
19 bainitic-holding step, consist of a lamellar microstructure, which is light gray or white
20 and identified as the RA phase in Figs. 3b-3g. These RA regions co-exist with the
21 strip-like ferrite around them that forms the bainite phase. It is also recognized that
22 the bainite, exhibiting granular and wormlike microstructures, mainly co-exists with
23 RA and distributes around the ferrite. While the content of RA increases with the
24 increase in the annealing temperature from 750°C to 880°C (Figs. 2b–e), the bainite
25 content reaches a maximum at the annealing temperature of 820°C for 120 s, with a

1 subsequent bainitic holding at 400°C for 300s (steel C, Fig. 2c).

2 Experimental data for the RA volume fraction obtained by various
3 experimental techniques for all the steels are summarized in Fig. 4. Three samples
4 under the same heat-treatment process are used for each measurement method to
5 obtain the statistical variations of the RA volume fraction, as shown in Fig. 4. The
6 results in Fig. 4 reveal the experimental discrepancies among the different probing
7 techniques. For example, the VSM-measured RA volume fraction is consistently
8 higher than those obtained by SEM, XRD, and EBSD. The major reason for this
9 systematic deviation is attributed to the respective resolution limitations of SEM and
10 XRD: The former cannot probe RA with ultrafine size due to the measurement
11 resolution, while the latter cannot detect the interior of the sample. The magnetic
12 measurement, which can probe 3 mm bulk material, leads to a more accurate
13 volumetric result.

14 Even when considering these measurement-to-measurement and
15 sample-to-sample discrepancies, a consistent trend can be observed from Fig. 4
16 concerning the effects of the heat-treatment parameters on the resulting RA volume
17 fractions. The volume fraction of RA increases monotonically with the increase in the
18 annealing temperature, due to the decrease in the primary ferrite resulting from the
19 higher austenitizing temperature. Another reason is related to the variation of the
20 carbon concentration in the austenite, affecting its thermal stability [8]. A careful
21 measurement of the austenite lattice parameter can determine reliably the carbon
22 content [26, 33-35]. A previous study [26] indicated that the average carbon content of
23 RA slightly decreases with its increasing volume fraction, following the higher
24 annealing temperature. The bainitic-holding temperature also plays a key role in
25 influencing the RA content. For example, when keeping the annealing temperature

constant at 850°C, the RA volume fraction increases from 19% to 21% (XRD average) with an increase in the bainitic-holding temperature from 400°C (steel D) to 420°C (steel F). However, a further increase of the bainitic-holding temperature to 450°C (steel G) led to a noticeable drop in the RA content to 18%. Among all samples, steel F, which was held at a bainitic temperature of 420°C for 300s, has the highest RA content. The RA contents are considerably lower in steels A (Fig. 3a) and H (Fig. 3h), compared with those in other steels.

No lamellar microstructure features were observed in steels A and H, whereas salient bainitic lamellar microstructures are consistently observed in other samples. Zaefferer et al. [39] identified and quantified the bainite in TRIP-assisted steels using EBSD analysis. They showed that bainite exhibits a granular form in an Al-containing TRIP steel, whereas it assumed a more lamellar morphology in Si-alloyed TRIP steels. Thus, it is conceivable that in the present study, the appropriate heat-treatment process to obtain the maximum RA is an annealing treatment at 850°C for 120s, followed by bainitic holding at 420°C for 300s. In addition, it should be noted that a small amount of RA is inevitably transformed into martensite during the cooling process without bainitic holding, resulting in a complex microstructure consisting of martensite, bainite and RA. Consequently, it is difficult for SEM analysis alone to discern the complexity of RA and martensite. A series of EBSD measurements were further conducted to confirm the effect of the different heat-treatment processes on the variation of the microstructures in the steels. The results in Fig. 4 demonstrate that the bainitic-holding process effectively promotes the formation of the RA phase.

3.2. *Effects of RA volume fraction and morphology on macroscopic properties*

3.2.1. Measured tensile properties

As discussed above, steels C, F, and H have different RA contents, namely, 16 vol.%, 23 vol.%, and 10 vol.%, respectively, according to the VSM data displayed in Fig. 4. Therefore, it is conceivable that the associated mechanical properties of these three steels should also exhibit significant differences. Fig. 5 shows the measured true stress–true strain curves for the three steels. Steel C with a medium RA content has the highest elongation to failure (ε_f) of 50%, along with the highest yield stress (σ_y) of 510 MPa and UTS of 1,100 MPa. On the other hand, steel F with the highest RA content shows a σ_y of 437 MPa and a UTS of 943 MPa as well as a slightly decreased ε_f of 48%. Steel H, annealed at 850°C for 120 s without the bainitic-holding process, exhibits the lowest ε_f of 39%, along with the lowest σ_y of 340 MPa and the lowest UTS of 800 MPa.

These results indicate that the excellent combination of high strength and good ductility for steel C is related not only to its higher RA content but also to its morphology, dispersion, and stability.

3.2.2. Effects of RA morphology and distribution

To further explore the effect of RA morphologies on the mechanical properties, systematic TEM observations were performed on samples obtained from various heat-treatment conditions. Numerous TEM observations have been performed on grains with crystallographic $\langle 110 \rangle$ orientation to evaluate the distribution and content of RA, despite of the limited precision of this approach. In this orientation, (-111) and $(1-11)$ RA grains are positioned edge-on, while (111) and $(11-1)$ RA grains are inclined to the surface, ensuring reliable measurements of the RA thickness/diameter along the $[110]$ beam direction. Thus, to some extent, representative results of the RA volume fraction can also be obtained from TEM observations, which are included in Fig. 4.

The typical microstructures for steels C, F, and H are shown in Fig. 6. The corresponding selected-area-electron-diffraction (SAED) patterns for the circled RA in steels F and H are shown in the inset of Figs. 6c and 6f, respectively. In Figs. 6a–d, many RA films exhibit a multi-scale microstructure with a size of 100 – 400 nm in thickness and 2 – 5 μm in length, separated by bainitic ferrite (BF) plates. In contrast, the RA in steel H typically assumes a more blocky configuration with a size of several microns (Fig. 6e). The corresponding SAED pattern is shown in Fig. 6f. The results reveal that steels C, F, and H have a RA thickness of 200 ± 30 nm, 350 ± 40 nm, and $1,500 \pm 300$ nm, respectively. Obviously, the bainitic-holding process is important to realize multi-phase microstructures with ultrafine RA lamellae. Recently, the influence of the morphology on the stability of RA in a Q&P steel has been reported by Xiong et al. [27], revealing that the film-like RA, despite of having a much lower carbon content, is stable up to a strain of 12%, while the blocky RA with a high carbon content promotes the martensite transformation already at the onset of plastic deformation. The authors attributed the morphology effects in the RA stability during deformation to the properties and the morphology of the surrounding matrix. For example, the mechanical stability of RA against straining is higher, if RA islands are surrounded and shielded by hard martensite.

In order to examine the effects of the RA morphology on its stability during the deformation process, interrupted tensile tests are performed in conjunction with EBSD for steels, C and H, with 10% strain increments. Fig. 7 shows the evolution of the fcc phase in steels C and H during deformation with increasing strain. We observe that the RA content of steel C (with lath RA) gradually decreased with increasing strain and finally exhausted at a strain above 40%. The blocky RA in steel H dramatically decreased 10% strain to only a few percent, and almost completely

disappeared after a true strain of 20%, underlining the role of the austenite stability on the overall mechanical response of the materials.

3.2.3. Effects of RA carbon content and stability

For steel C, obtained by the annealing and bainitic-holding processes, the most prominent characteristic is its lamellar RA with an average thickness (D) of only 200 ± 30 nm and a length of several microns, which is divided by ferrite platelets (Figs. 6a–b). This characteristic microstructure is very beneficial for concurrently improving the ductility and strength in the TRIP-assisted steels [26]. However, one may note that steel F exhibits an inferior combination of strength and ductility, compared with steel C, though it has the higher RA content and similar topological multiphase microstructure features containing also fine lamellar RA ($D = 350 \pm 40$ nm). Hence, there are other factors determining the mechanical properties of the TRIP-assisted steel through the gradual-deformation-induced martensitic-phase transformation. In other words, the RA stability, which is mainly determined by its carbon content should be closely connected with the local composition and deformation process in TRIP-assisted steels [9], as was recently also demonstrated by corresponding atom probe observations [28, 40]. It has been confirmed that RA with a low carbon concentration transforms to martensite more rapidly during straining, leading to less increase in elongation [41].

The XRD analysis shows that the RA-carbon concentrations (in wt.%) are 1.1%, 0.8% and 0.6% for steels C, F and H, respectively.

Indeed, steel C with its moderate RA volume fraction has a high carbon concentration, whereas steel F with the highest RA fraction has a lower carbon concentration, and steel H which was synthesized without bainitic holding has the lowest carbon concentration. When comparing steels C and F with their similar RA

1 morphology, we observe that the carbon concentration of RA in steel F is lower due to
2 its higher RA volume fraction. However, steel C has a higher RA volume fraction
3 and RA carbon content than steel H, owing to the fine lamellar RA structure resulting
4 from the bainitic-holding process. The underlying reason for this effect is that the
5 dispersion of the microstructure effectively lowers the necessary diffusion distance of
6 carbon, accelerating the diffusion of carbon into a neighbored lamellar RA, and
7 subsequently increasing its stability. It is conceivable that the RA with the highest
8 carbon concentration (steel C) must possess the highest stability, enable slower and
9 more gradual martensite transformation during deformation, as shown in Fig. 7,
10 leading to the best strength and ductility combination.

11 On the other hand, the contribution of the BF on the strength cannot be
12 ignored because BF is mechanically stronger than ferrite due to its higher carbon
13 content. A Gaussian multi-peak fitting method was employed to de-convolute the (211)
14 peaks of the ferrite in different steels, Fig. 8. The obtained sub-peaks, shown as short
15 dashed curves, and dashed dot curves correspond to the ferrite with a larger lattice
16 parameter (the high carbon content indicates BF) and a smaller lattice parameter (the
17 low carbon content indicates ferrite), respectively. This observation reveals that the
18 BF volume fraction is significantly higher in steel C, in comparison to steels F and H.
19 This observation is consistent with the TEM observations in Fig. 6 and SEM
20 observations in Fig. 3.

21 3.2.4. Strain distribution and deformation compatibility during deformation

22 In order to further illustrate the benefits associated with the stable RA during
23 the entire deformation process, interrupted tensile tests were carried out for steels C
24 and H with a strain increment of 10%, indicated by the dotted symbols in the tensile

curves of Fig. 5. Subsequently, the deformed microstructures are investigated by EBSD and KAM analysis, and the results for steel C are presented in Fig. 9.

Illustrated as inverse-pole-figure (IPF) maps (Figs. 9a–e), the ferrite grains are elongated along the tensile direction with gradually increasing strain, ranging from 10% to 40%. For example, the average aspect ratio of grains is 2.1, 2.6, 3.0 and 3.7 for a strain of 10%, 20%, 30% and 40%, respectively. However, this value slightly decreases from 3.7 to 3.2 as the strain further increases from 40% to 50%, due to an increase in the fraction of small angle boundaries. The misorientation analysis indicated that the ratio of grains bearing small-angle boundaries increases from 30% to 45%. Nevertheless, when referring to the inset of Fig. 9a, no obvious texture effect was observed during deformation of steel C. A good way to observe orientation changes caused by plastic deformation is the KAM function, which is a measure of local orientation changes, such as those introduced during deformation associated mainly with the in-grain dislocation activity [41]. Studying the KAM evolution as a function of strain reveals the deformation activity, because the increment in the KAM measure is closely related to the increasing dislocation density. The KAM maps (Figs. 9a1–e1) were also progressively obtained at each interrupted strain level for the same location of the steel by analyzing the corresponding EBSD maps (Figs. 9a–e), illustrating the strain distribution evolution during the entire deformation process.

At lower strain levels, the local misorientation developed inhomogeneously and appeared high near grain boundaries and triple junctions, as indicated by the green contour lines in the figures. At a strain level of 0.1, grain boundaries showed higher KAM values, while grain interior regions remained nearly unchanged (blue contours) relative to the undeformed state (Fig. 9a1). With increasing straining, the magnitude of the local misorientation increased, being significantly higher at grain

1 boundaries than inside the grain interiors, indicating that the near-grain boundary
2 regions suffered the majority of the deformation (Figs. 9b1–c1). Fleck et al. [42] and
3 Demir et al. [43] noted that the higher KAM at grain boundaries reflects the formation
4 of geometrically-necessary dislocations accommodating the evolving strain gradients
5 between two grains.

6 With further deformation, the regions of higher KAM values not only
7 gradually increased at grain boundaries but also extended into the grain interiors (Fig.
8 9d1). At the highest strain level of 0.5, the green area is as high as 90%, suggesting
9 rather homogeneous deformation at this strain level. Combined with OM and SEM
10 observations, it is conceivable that at the initial stage of deformation, the
11 transformation of austenite into martensite played a key role because the RA was
12 always located in the vicinity of prior grain boundaries. With progressive straining,
13 the interaction and competition among ferrite, BF, and the transformation product
14 martensite, took over and dominated the deformation, resulting in a more
15 homogeneous deformation and an excellent resulting combination of strength and
16 ductility.

17 Correspondingly, the evolution of the KAM distribution at different strains
18 was analyzed, as shown in Fig. 10. The results revealed different characteristics: For
19 low strains up to 10%, not only the KAM peak was the lowest but also the distribution
20 was the most narrow one. With increasing strain, the KAM peak fraction slightly
21 increased, and the peak distribution broadened, i.e., the KAM distribution shifted to
22 an overall higher mean value. This scene can be attributed to the
23 deformation-induced-martensitic transformation from austenite throughout the
24 deformation process and the deformation of ferrite at higher strain levels. It is well
25 established that the variation of the KAM is sensitive to the dislocation characteristics

1 and density [42, 44]. Dislocation cells are mainly structural features of deformed
2 ferrite due to wavy glide, resulting in low intragranular misorientation to weakly
3 affect the evolution of the KAM distribution with increasing strain [45]. On the other
4 hand, more planar glide caused by the partial dislocations dominates the deformation
5 of austenite [46-49], leading to the higher local (intragranular) interior stress.
6 Consequently, the KAM values of the austenite and its correspondingly increasing
7 change rate might be higher than those observed for the ferrite at the same strain level.
8 In addition, with progressing strain, the gradually and newly formed martensite has
9 the highest KAM value, related to the displacive transformation mechanism and its
10 higher hardness, compared to soft austenite and ferrite. Thus, it is reasonable that both,
11 the KAM distribution and the peak values increase with increasing strain levels.

12

13 3.3 *Deformation mechanisms and strategy for property improvements*

14 During deformation of multiphase TRIP-assisted steels, the local stress
15 concentrations due to the high hardness of the newly-formed martensite increase with
16 straining and are responsible for the initiation and formation of defects and flaws. It is
17 well proven that voids and cracks easily form in materials with a large difference of
18 strength between the matrix (ferrite) and second phase (martensite) [12, 50, 51]. Thus,
19 the poor combination of strength and strain for steel H should be associated with the
20 decreasing TRIP-assisted effect, which results from the inhomogeneous deformation
21 of the blocky RA, the low RA volume fraction, as well as the low stability of RA.

22 In contrast, the ultrafine RA lamellae, which have appropriate stability and a
23 high dispersion inside the surrounding BF matrix, have been proven as beneficial for
24 promoting a more steady and gradual martensitic transformation, retarding the
25 initiation of voids/cracks, hence, providing a continuous work-hardening effect and

1 enhanced ductility by delaying the onset of local necking. The deformed
2 morphologies of steels C and H are investigated, using TEM observations, as revealed
3 in Fig. 11a–b. Clear differences can be seen for the deformation behaviors of steels C
4 and H. Firstly, the dislocation density is significantly higher in the deformed steel C
5 (Fig. 11a), indicating the more homogenous and severe local plastic deformation
6 before failure. The corresponding deformation mechanisms of steels C and H are
7 explained, using the schematic illustrations given in Fig. 11c and 11d, respectively.

8 Nevertheless, the TRIP-assisted steels do not have a homogeneous
9 microstructure in general, and the factors influencing mechanical properties of the
10 TRIP-assisted steel may be complex, multiple, and synergistic. Using in-situ neutron
11 diffraction, Tomota *et al.* [4] reported that stress-induced-martensitic transformation
12 occurs during plastic deformation but a considerable amount of austenite prevails
13 even after the onset of necking. It is concluded that the contribution of the
14 transformation strain is negligible, due to the RA bearing about 1.0 wt.% C. At the
15 same time, Timokhina *et al.* [52] confirmed that mechanical properties of TRIP steels
16 with and without Nb depend on both the individual behavior of all phases and the
17 interaction between the phases during deformation. For instance, the polygonal ferrite
18 and bainite of the C-Mn-Si steel provide a larger contribution to the elongation than
19 that of the C-Mn-Si-Nb steel. The mechanical stability of the RA against straining
20 depends on its location within the microstructure, the morphology of the bainite, and
21 its interaction with other phases during straining. By meticulously monitoring the
22 local intra-granular misorientation, it was concluded that the bcc phases (ferrite and
23 bainite) take up the larger part of the nominal strain whereas the residual austenite
24 primarily responds to the mechanical load by a partial (stress-induced) martensite
25 transformation. Hence, the texture change observed in the RA could be attributed to

1 the orientation-selective character of the phase transformation [33]. On the other hand,
2 some RA grains with a high carbon content may not transform into martensite during
3 deformation, which is related to the fact that the increasing carbon content decreases
4 the start point of the martensite transformation and renders the RA too stable to
5 convert for increasing the thermal stability [53].

6 This study mainly focuses only on exploring the fundamental factors
7 influencing the ductility and strength of the TRIP steel. The morphology and content
8 of RA have been characterized, using various techniques, providing also a quantitative
9 comparison among various characterization techniques. The concurrent increase in the
10 elongation and strength of steel C demonstrates that the morphology, volume fraction,
11 and stability of RA are equally important in optimizing the ductility of TRIP-assisted
12 steels. The parallel ultrafine RA laths can effectively improve the strength and
13 ductility of TRIP-assisted steel concurrently. In general, the property improvement
14 steps taken in this study are schematically summarized in Fig. 12. The salient feature
15 of the present strategy mainly lies in tailoring the heat-treatment parameters to
16 concurrently control the volume fraction, morphology, and carbon content of the RA.

18 **4. Summary**

19 With a suite of multi-modal and multi-scale characterization techniques, the
20 present study unambiguously proves that an excellent combination of ultrahigh
21 strength and good ductility can be achieved by tailoring the inter-grain/phase
22 microstructures. By designing the heat-treatment processes, both the strength and
23 ductility of TRIP-assisted steels can be improved concurrently due to the design of
24 ultrafine-lamellar RA with high mechanical stability against straining. The main result
25 can be summarized as follows:

1 1. Ultrafine-lamellar RA has been obtained by intercritical annealing and
2 bainitic holding, while the heat treatment excluding bainitic holding only results in
3 blocky RA. The volume fraction of RA after different heat treatments has been
4 studied, using various methods, including XRD, OM, SEM, EBSD, magnetic
5 characterization, and TEM. The results demonstrate that the volume fraction of RA is
6 closely associated with the heat-treatment processes. Among the different methods,
7 the magnetic measurement shows the highest precision to determine the volume
8 fraction of RA. TEM is the most effective method to differentiate the ultrafine RA
9 lamellae from the ferrite platelet and the blocky RA.

10 2. The RA volume fraction and carbon concentration (in wt.%) are 16%/1.1%,
11 23%/0.8% and 10%/0.6% for steels C, F and H, respectively. Conventional uniaxial
12 tensile tests showed that steel C with a medium RA content has the highest ε_f of 50%,
13 along with the highest σ_y of 510 MPa and the highest UTS of 1,100 MPa. However,
14 steel F with the highest RA content has a lower σ_y of 437 MPa and UTS of 943 MPa
15 as well as a decreased ε_f of 48%. Steel H annealed at 850°C for 120 s without the
16 bainitic-holding process exhibits the lowest ε_f of 39%, along with the lowest σ_y of 340
17 MPa and the lowest true stress of 800 MPa.

18 3. Interrupted uniaxial tensile tests, incorporated with the EBSD and KAM
19 analyses, have been employed to investigate the mechanical stability of RA against
20 strain loading. The transformation rate of the RA into martensite was not only related
21 to the initial fraction but also affected by the strain level. The RA in steel C has the
22 higher mechanical resistance against strain than that in steel H. The results proved that
23 the RA stability is mainly dominated by its morphology and carbon concentration. In
24 addition, the RA stability against strain may be affected by the morphology of the
25 matrix. The high BF content of steel C was associated with the high strength.

4. By controlling the morphology, distribution, and stability against strain of the RA, we can improve the mechanical properties of the TRIP-assisted steels to achieve both high strength and high ductility. The ultrafine RA lamellae, which have appropriate stability and high dispersion within the BF matrix, are very beneficial for a steady and gradual martensitic transformation, retarding the initiation of local strain concentrations, hence providing a continuous work-hardening effect. In contrast, the blocky RA may play a major role for the initiation of voids and cracks, due to the low stability facilitating an abrupt transformation of RA into martensite. The large size of the newly formed hard martensite is detrimental for coordinating the intergranular deformation, resulting in a poor combination of strength and ductility. These detailed findings and the associated strategies will help the future endeavors in simultaneously improving the strength and ductility of this class of materials.

Acknowledgements

This research is supported by the National Natural Science Foundation of China (Grant Nos. U1430132, 51231002), the National Science and Technology Support Project (2011BAE13B03), and the Fundamental Research Funds for the Central Universities (N130402005). Pacific Northwest National Laboratory is operated by Battelle for the U.S. Department of Energy (DOE) under Contract no. DE-AC05-76RL01830. X. Sun's contribution to this work is funded by DOE's Vehicle Technologies Office under the Automotive Lightweighting Materials Program managed by Mr. William Joost.

References:

- [1] P.J. Jacques, E. Girault, A. Mertens, B. Verlinden, J. Van Humbeeck, F. Delannay, ISIJ Int. 41 (2001) 1068–74.
- [2] P.J. Jacques, Curr. Opin. Solid State Mater. Sci. 8 (2004) 259–71
- [3] F.G. Caballero, H.K.D.H. Bhadeshia, Curr. Opin. Solid State Mater. Sci. 8 (2004) 251–57.
- [4] S. Li, R. Zhu, I. Karaman, R. Arroyave, Acta Mater. 60 (2012) 6120–30.
- [5] D. Edmonds, D. Matlock, J. Speer, In: Y. Weng, et al. eds., Advanced steels, (2011) p. 241–53.
- [6] S. Zaefferer, J. Ohlert, W. Bleck, Acta Mater. 52 (2004) 2765–78.
- [7] F. Lani, Q. Furnemont, T. Van Rompaey, F. Delannay, P.J. Jacques, T. Pardoen, Acta Mater. 55 (2007) 3695–705.
- [8] M-M. Wang, C.C. Tasan, D. Ponge, A. Kostka, D. Raabe, Acta Mater. 79 (2014) 268–81.
- [9] K.S. Choi, A. Soulami, W.N. Liu, X. Sun, M.A. Khaleel, Comp. Mat. Sci. 50(2010) 720–730.
- [10] K. Sugimoto, N. Usui, M. Kobayashi, S. Hashimoto, ISIJ Int. 32 (1992) 1311–18.
- [11] P.J. Jacques, Q. Furnémont, T. Pardoen, F. Delannay, Acta Mater. 49 (2001) 139–52.
- [12] Y. Tomota, H. Tokuda, Y. Adachi, M. Wakita, N. Minakawa, A. Moriai, Y. Morii, Acta Mater. 52 (2004) 5737–45.
- [13] J.G. Speer, D.V. Edmonds, F.C. Rizzo, D.K. Matlock: Curr. Opin. Solid State Mater. Sci. 8 (2004) 219–37.
- [14] Q.X. Ran, Y.L. Xu, J. Li, J.Q. Wan, X.S. Xiao, H.F. Yu, L.Z. Jiang, Mater. Design 56 (2014) 959–65.
- [15] J. Bouquerel, K. Verbeken, B.C. De Cooman, Acta Mater. 54 (2006) 1443–56.
- [16] P.J. Jacques, Q. Furnémont, F. Lani, Acta Mater. 55 (2007) 3681–93.
- [17] G. Lacroix, T. Pardoen, P.J. Jacques, Acta Mater. 56 (2008) 3900–13.
- [18] J.G. Speer, D.K. Matlock, B.C. De Cooman, J.G. Schroth: Acta Mater. 51 (2003) 2611–22.
- [19] D. Raabe, D. Ponge, O. Dmitrieva, B. Sander, Adv. Eng. Mater. 11 (2009) 547–55.
- [20] D. Raabe, D. Ponge, O. Dmitrieva, B. Sander, Scripta Mater. 60 (2009)

1 1141–44.

2 [21] O. Dmitrieva, D. Ponge, G. Inden, J. Millan, P. Choi, J. Sietsma, D. Raabe, *Acta*
3 *Mater.* 59 (2011) 364–74.

4 [22] E. Melero, N.H. Van Dijk, L. Zhao, J. Sietsma, S.E. Offerman, J.P. Wright, S.
5 Van der Zwaag, *Acta Mater.* 57 (2009) 533–43.

6 [23] J.G. Speer, F.C. Rizzo Assunc, D.K. Matlock, D.V. Edmonds: *Mater. Res.* 8
7 (2005) 417–23.

8 [24] D.V. Edmonds, K. He, F.C. Rizzo, B.C. De Cooman, D.K. Matlock, J.G. Speer:
9 *Mater. Sci. Eng. A* 438-40 (2006) 25–34.

10 [25] T.D. Bigg, D.V. Edmonds, E.S. Eardley, J. Alloy *Compd.* 585 (2013) S695–S698.

11 [26] Y.F. Shen, Y.D. Liu, X. Sun, Y.D. Wang, L. Zuo, R.D.K. Misra, *Mater. Sci. Eng.*
12 *A* 583 (2013) 1–10.

13 [27] X.C. Xiong, B. Chen, M.X. Huang, J.F. Wang, L. Wang, *Scripta Mater.* 68 (2013)
14 321–24.

15 [28] Y. Toji, H. Matsuda, M. Herbig, P.-P. Choi, D. Raabe, *Acta Mater.* 65 (2014)
16 215–28.

17 [29] R. Petrov, L. Kestens, A. Wasilkowska, Y. Houbaert, *Mater. Sci. Eng. A* 447
18 (2007) 285–97.

19 [30] R. Petrov, L. Kestens and Y. Houbaert: *Mater. Sci. Forum*, 550 (2007) 265–71.

20 [31] A. Grajcar, K. Radwanski, H. Krzton, *Solid State Phenomena*, 203-204 (2013)
21 34–37.

22 [32] M.-M. Wang, C.C. Tasan, D. Ponge, A.-Ch. Dippel, D. Raabe; *Acta Mater.*
23 (2014), In press

24 [33] L. Cheng, A. Böttger, T. de Keijser, E.J. Mittemeijer. *Scripta Mater.* 24 (1990)
25 509–14.

26 [34] N.H. van Dijk, A.M. Butt, L. Zhao, J. Sietsma, S.E. Offerman, J.P. Wright, *Acta*
27 *Mater.* 53 (2005) 5439–47.

28 [35] D.J. Dyson, B. Holmes, *J Iron Steel Inst.* 208 (1970) 469–74.

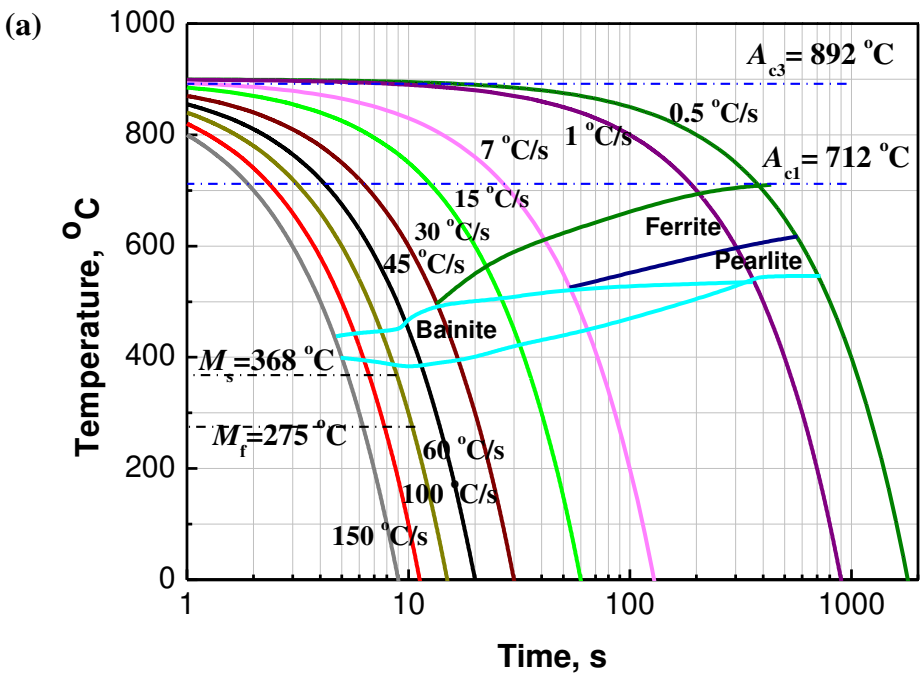
29 [36] L. Zhao, N.H. van Dijk, E. Brück, J. Sietsma, S. van der Zwaag, *Mater. Sci. Eng.*
30 *A* 313 (2001) 145–52

31 [37] B.D. Cullity, *Introduction to Magnetic Materials*, Addison-Wesley, Reading, MA,
32 1972.

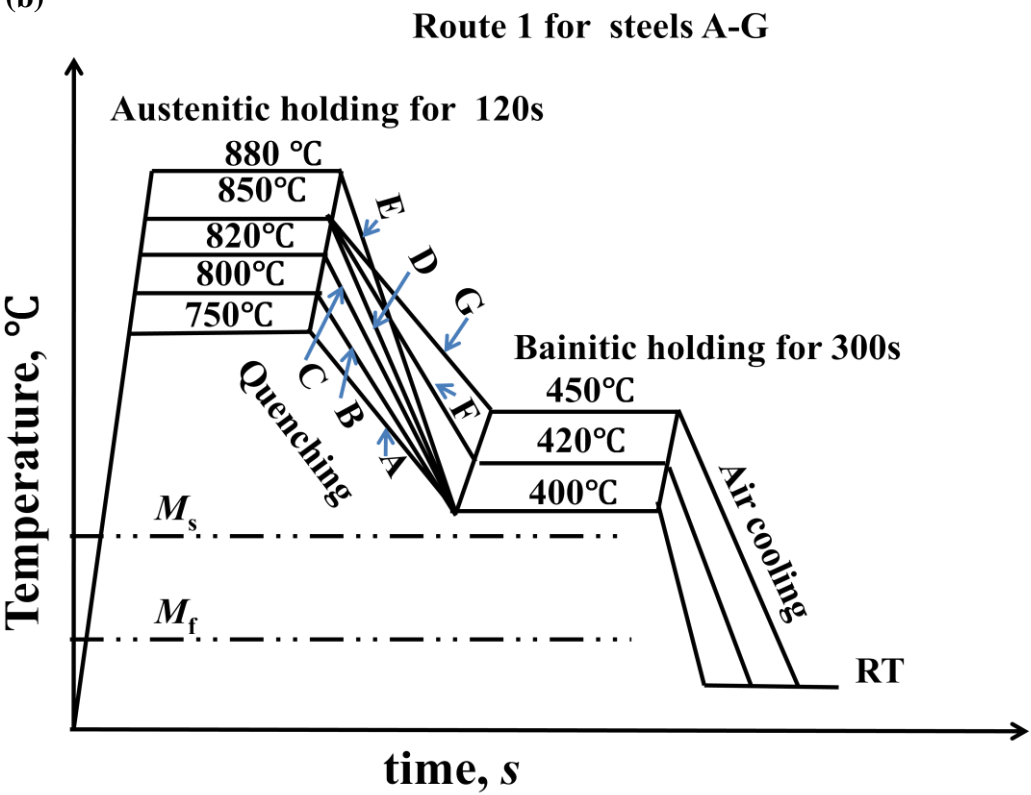
33 [38] J. Angeli, E. Früder, M. Panholzer, A.C. Kneissl, *Prakt. Metallogr.* 43 (2006)
34 489–04

- 1 [39] S. Zaefferer, P. Romano, F. Friedel, J. Microsc. 230 (2008) 499–08.
- 2 [40] J.-B. Seol, D. Raabe, P.-P. Choi, Y.-R. Im, C.-G. Park, Acta Mater. 60 (2012)
- 3 6183–99.
- 4 [41] M. Calcagnotto, D. Ponge, E. Demir, D. Raabe, Mater. Sci. Eng. A 527 (2010)
- 5 2738–46.
- 6 [42] N.A. Fleck, G.M. Muller, M.F. Ashby, J.W. Hutchinson, Acta Metall. Mater. 42
- 7 (1994) 475–87.
- 8 [43] E. Demir, D. Raabe, N. Zaafarani, S. Zaefferer, Acta Mater. 57 (2009) 559–569.
- 9 [44] C. Herrera, D. Ponge, D. Raabe, Acta Mater. 59 (2011) 4653–64.
- 10 [45] J.Y. Choi, J.H. Ji, S.W. Hwang, K.-T. Park, Mater. Sci. Eng. A 535 (2012) 32–39.
- 11 [46] V. Herold, H.-P. Karnthaler, Acta Metall. 37 (1989) 2177–83.
- 12 [47] D.A. Hughes, Acta Metall. Mater. 41 (1993) 1421–30.
- 13 [48] G. Winther, D. Juul Jensen, N. Hansen, Acta Mater. 45 (1997) 5059–68.
- 14 [49] M. Ojima, Y. Adachi, Y. Tomota, K. Ikeda, T. Kamiyama, Y. Katada, Mater. Sci.
- 15 Eng. A 527 (2009) 16–24.
- 16 [50] C. C. Tasan, J.P.M. Hoefnagels, M. Diehl, D. Yan, F. Roters, D. Raabe, Int. J.
- 17 Plast. 63 (2014) 198–210.
- 18 [51] C C Tasan, M. Diehl, D. Yan, C. Zambaldi, P. Shanthraj, F. Roters, D. Raabe,
- 19 Acta Mater. 81 (2014) 386–400.
- 20 [52] I.B. Timokhina, P.D. Hodgson, E.V. Pereloma, Metall. Mater. Trans. A, 35 (2004)
- 21 2331–41.
- 22 [53] J. Mahieu, J. Maki, B.C. De Cooman, S. Claessens, Metall. Mater. Trans. A 33
- 23 (2002) 2573–80.
- 24

Figures and Captions:



(b)



(c)

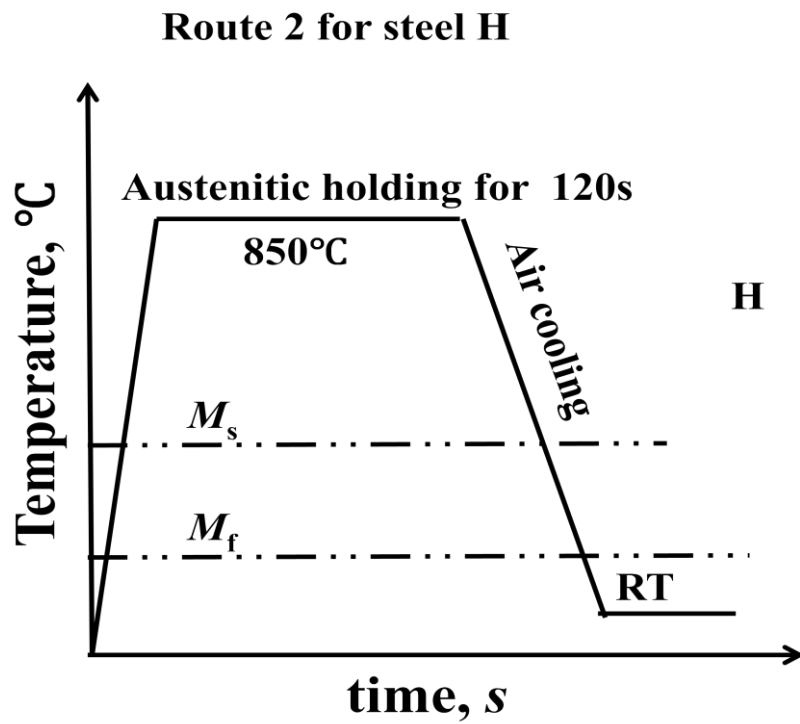


Fig. 1. Continuous-cooling-transformation (CCT) diagram determined for the investigated steel with the nominal chemical bulk composition of 0.19C-0.30Si-1.76Mn-1.52Al (wt.%) (a); schematic illustration of the different heat-treatment routes applied to steels A – G (b) and steel H (c), respectively.

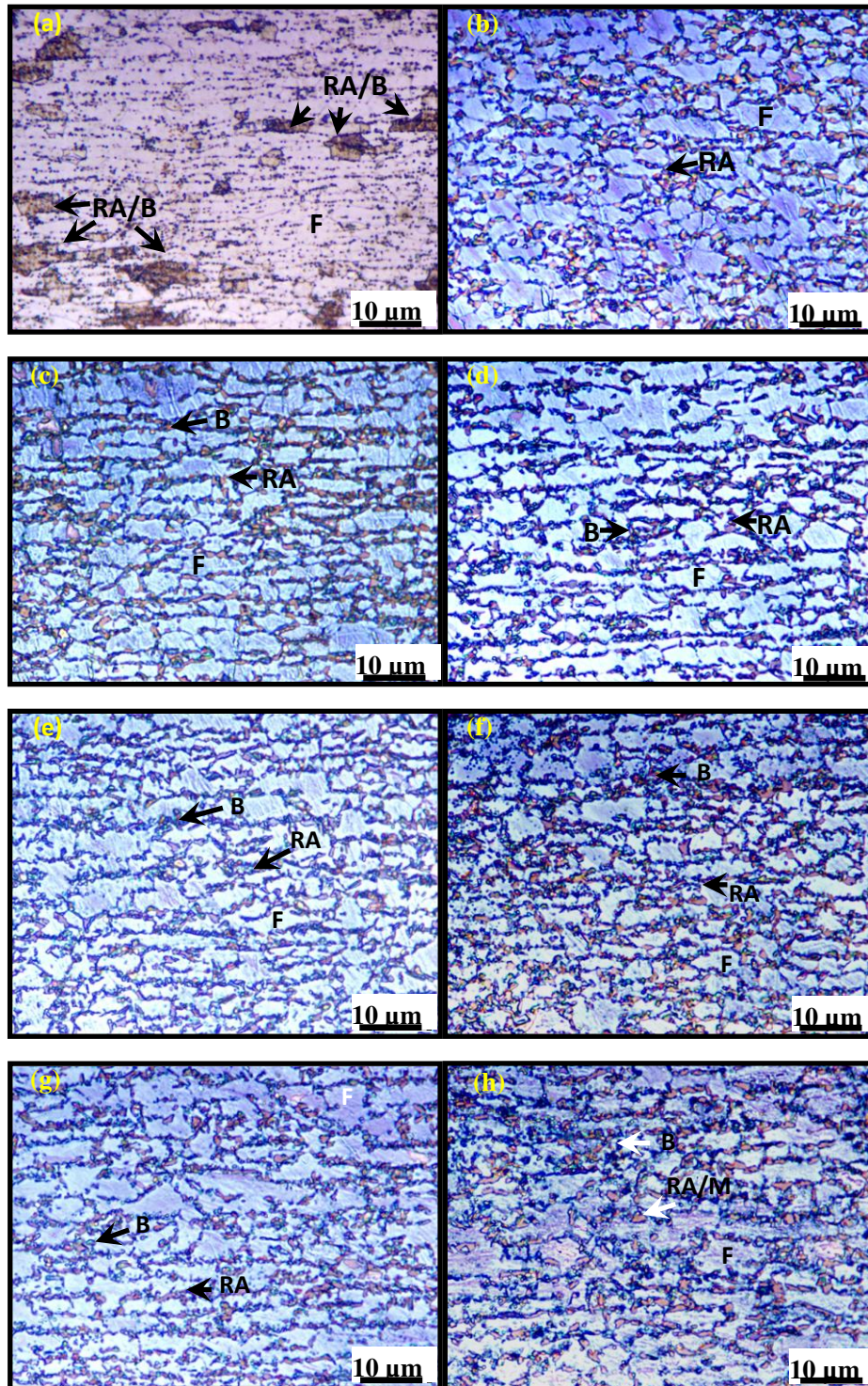


Fig. 2. Optical micrographs (a) – (h) obtained from steels A – H, respectively. F: ferrite; B: bainite; RA/B: retained austenite/bainite; RA/M: retained austenite/martensite.

Steel A: 750°C/120s + 400°C/300s; B: 800°C/120s + 400°C/300s; C: 820°C/120s + 400°C/300s; D: 850°C/120s + 400°C/300s; E: 880°C/120s + 400°C/300s; F: 850°C/120s + 420°C/300s; G: 850°C/120s + 450°C/300s; H: 850°C/120s.

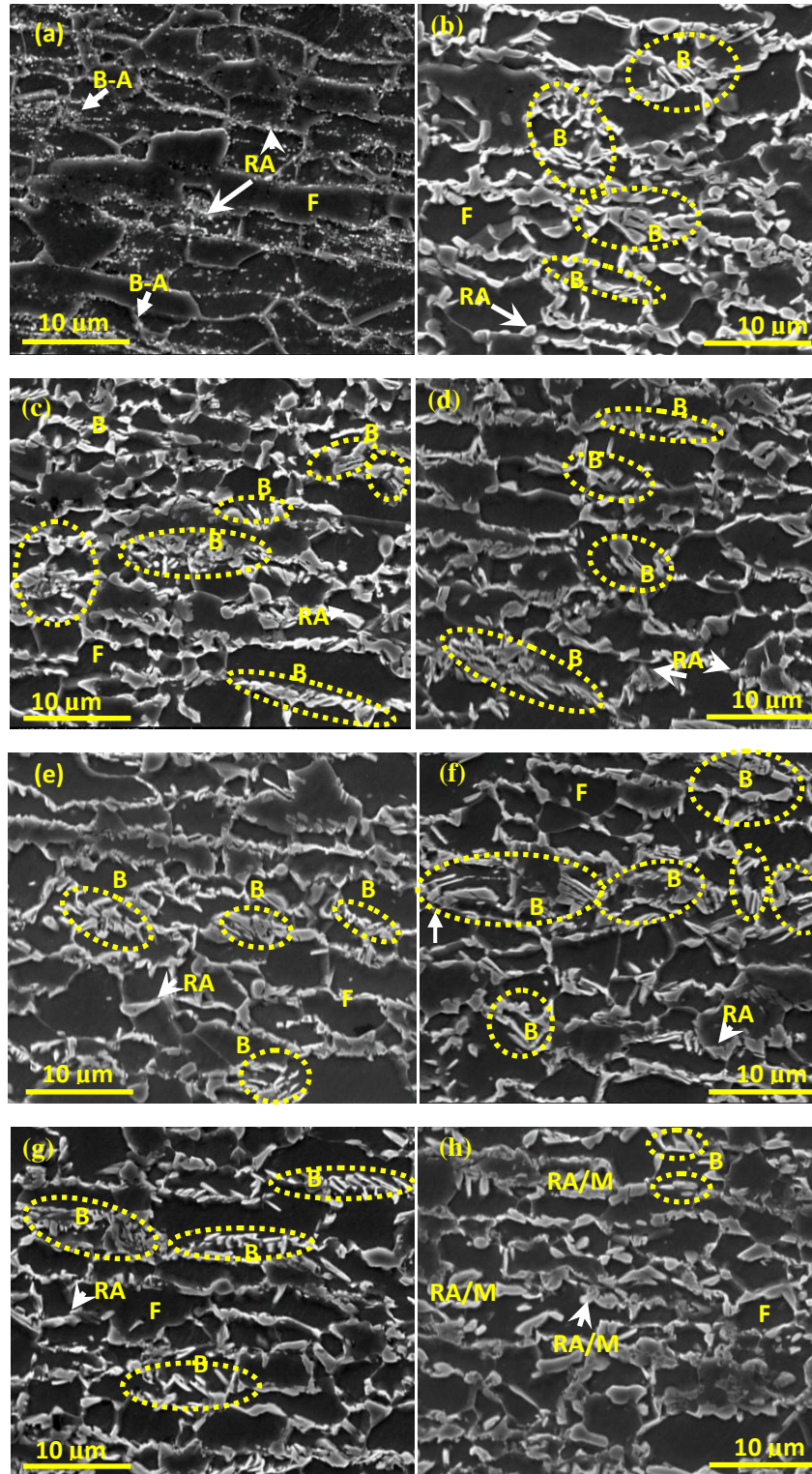


Fig. 3. SEM micrographs (a) – (h) as obtained from steels A–H, respectively. F: ferrite; B: bainite; RA: retained austenite/bainite; RA/M: retained austenite/martensite. Steel A: 750°C/120s + 400°C/300s; B: 800°C/120s + 400°C/300s; C: 820°C/120s + 400°C/300s; D: 850°C/120s + 400°C/300s; E: 880°C/120s + 400°C/300s; F: 850°C/120s + 420°C/300s; G: 850°C/120s + 450°C/300s; H: 850°C/120s.

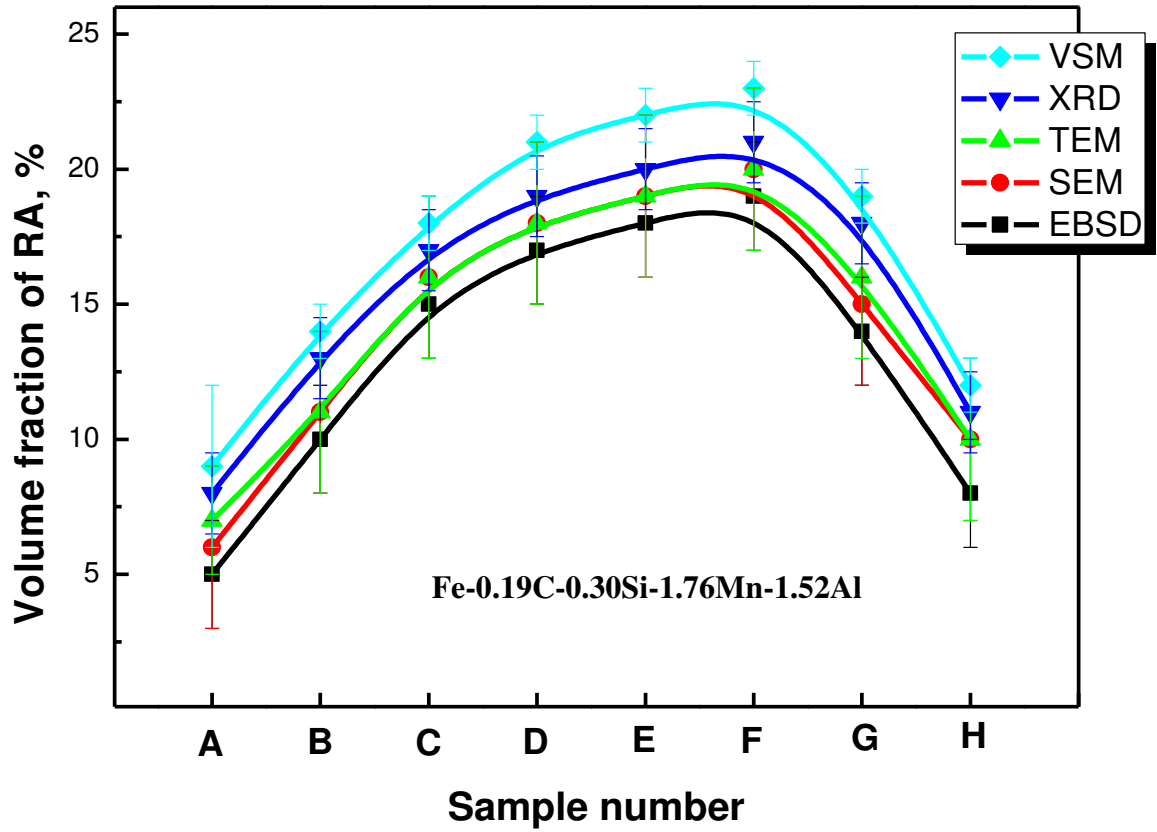


Fig. 4. Measured volume fraction of the retained austenite (RA) as a function of the heat-treatment process for steels A – H, identified by different measurement methods, including the vibration sample magnetometer (VSM), transmission-electron microscopy (TEM), X-ray diffraction (XRD), scanning-electron microscopy (SEM), and electron-backscatter-diffraction (EBSD). steel A: 750°C/120s + 400°C/300s; B: 800°C/120s + 400°C/300s; C: 820°C/120s + 400°C/300s; D: 850°C/120s + 400°C/300s; E: 880°C/120s + 400°C/300s; F: 850°C/120s + 420°C/300s; G: 850°C/120s + 450°C/300s; H: 850°C/120s.

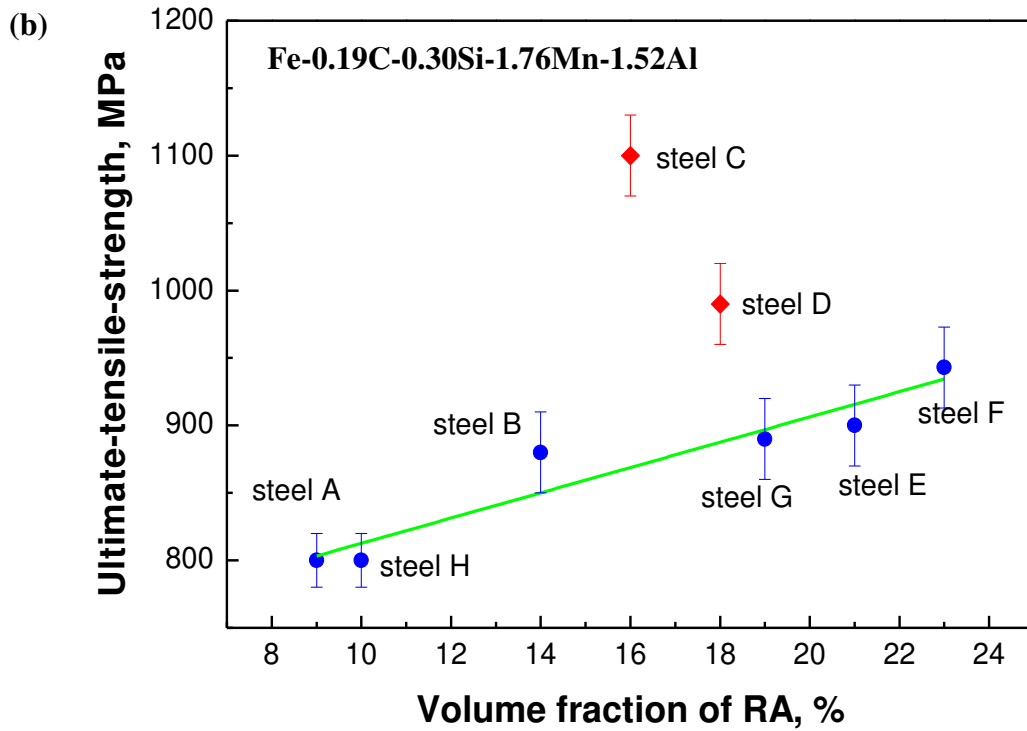
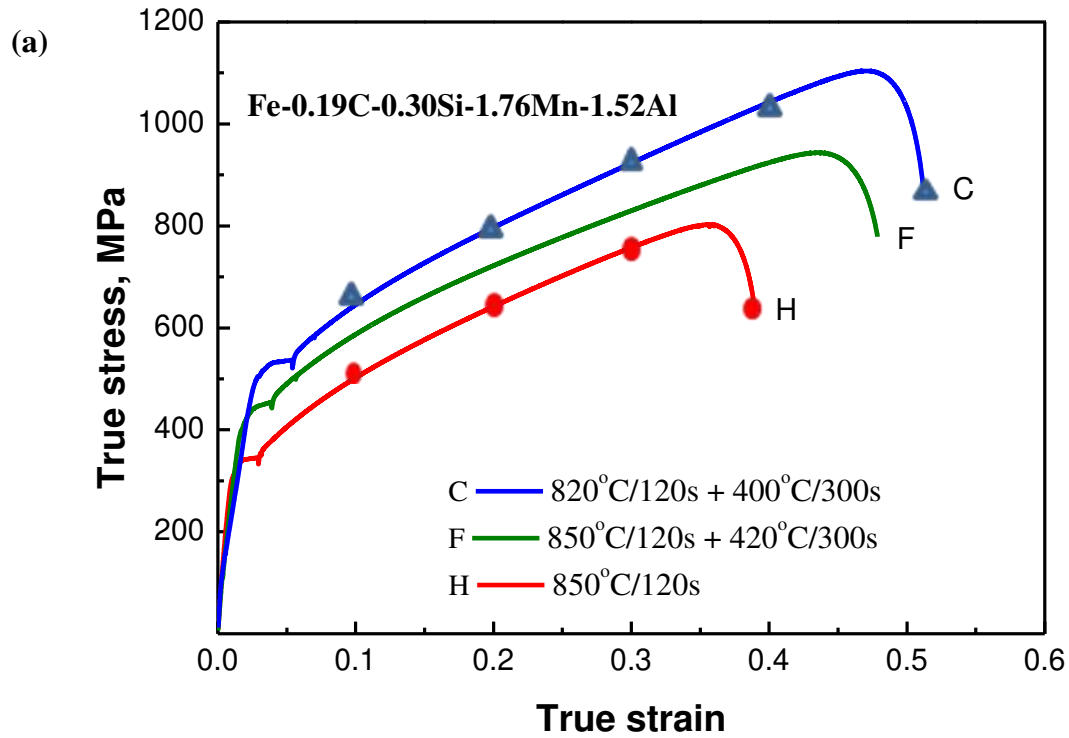


Fig. 5. (a) The true stress – true strain curves for steels C, F, and H with different heat-treatment processes. Steel C: 820°C/120s + 400°C/300s; F: 850°C/120s + 420°C/300s; H: 850°C/120s. (b) Ultimate-tensile-strength versus volume fraction of retained austenite (RA) for steels A–H.

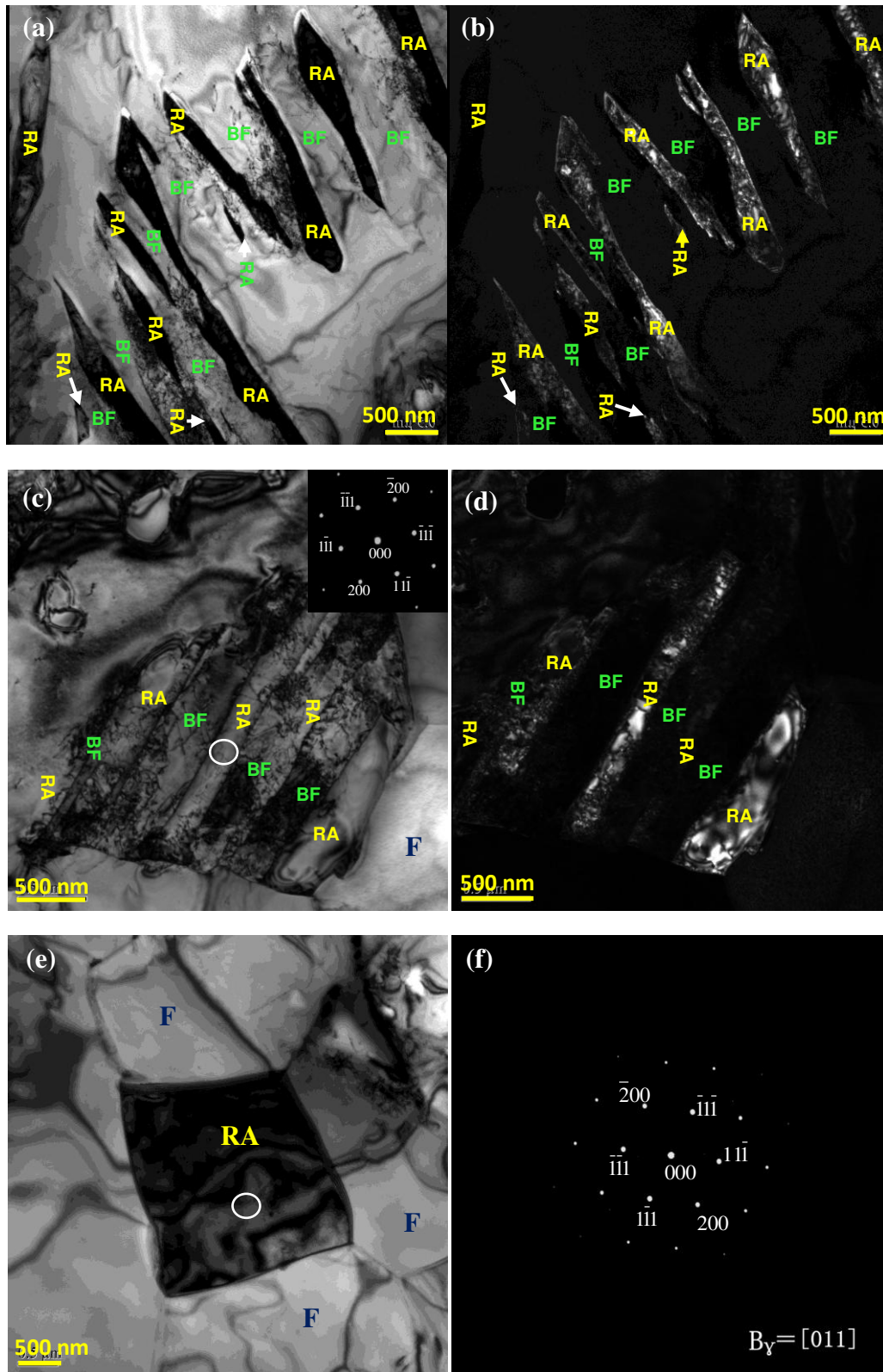


Fig. 6. TEM micrograph showing the morphology of retained austenite (RA) in steels C, F and H after heat-treatment. Bright- (a), (c) and dark-field (b), (d) images show that the bainite phase consists of bainitic-ferrite (BF) platelets and lamellar RA with a thickness of several hundred nanometers in steels C and F, respectively. The inset is

the corresponding SAED pattern indicated by the circle in (c). The blocky-type RA indicated by the circle (e) with the corresponding SAED pattern (f) for steel H without bainitic holding. Steel C: 820°C/120s + 400°C/300s; F: 850°C/120s + 420°C/300s; H: 850°C/120s.

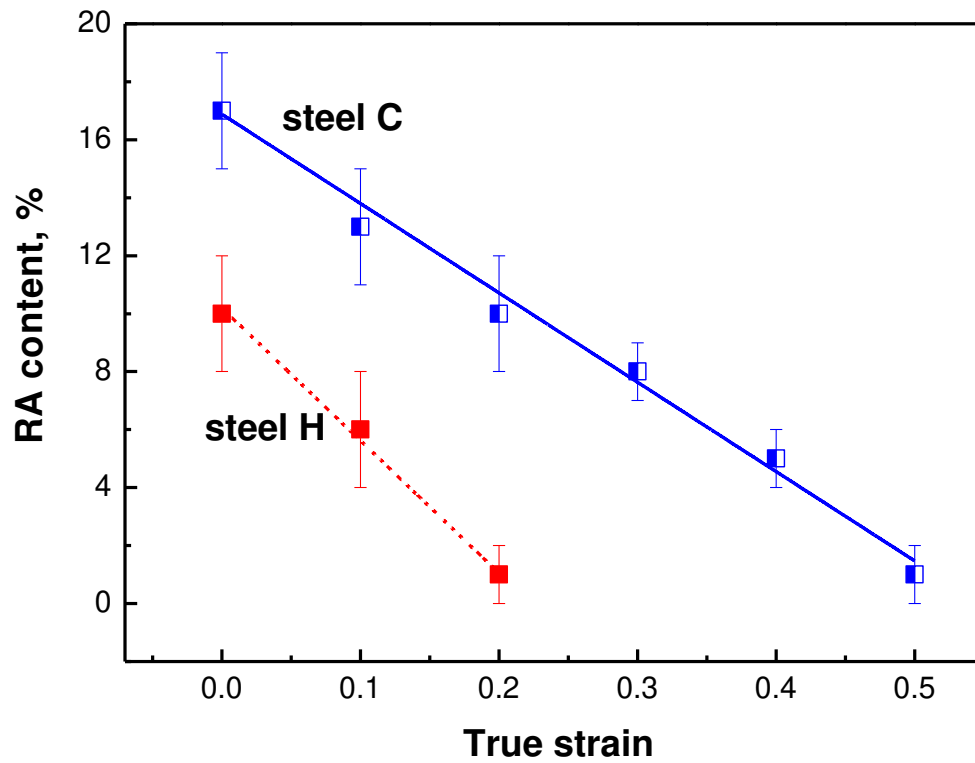


Fig. 7. Variations in the retained austenite (RA) content in steels C and H as a function of strain, as determined by EBSD. Steel C: 820°C/120s + 400°C/300s; H: 850°C/120s.

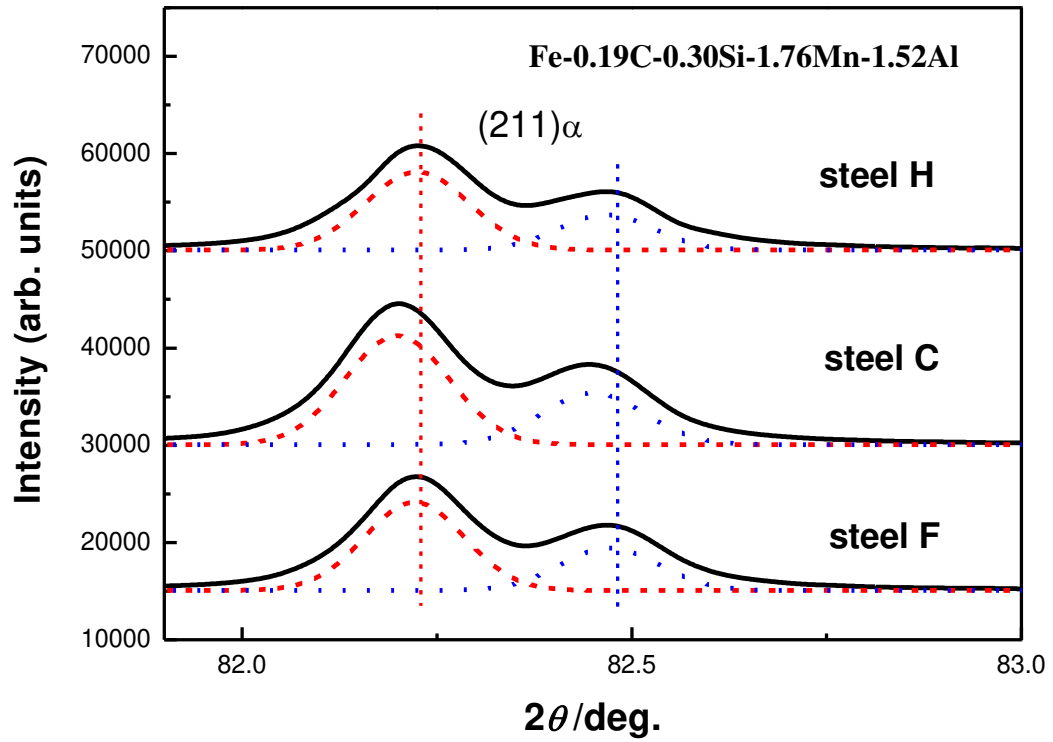
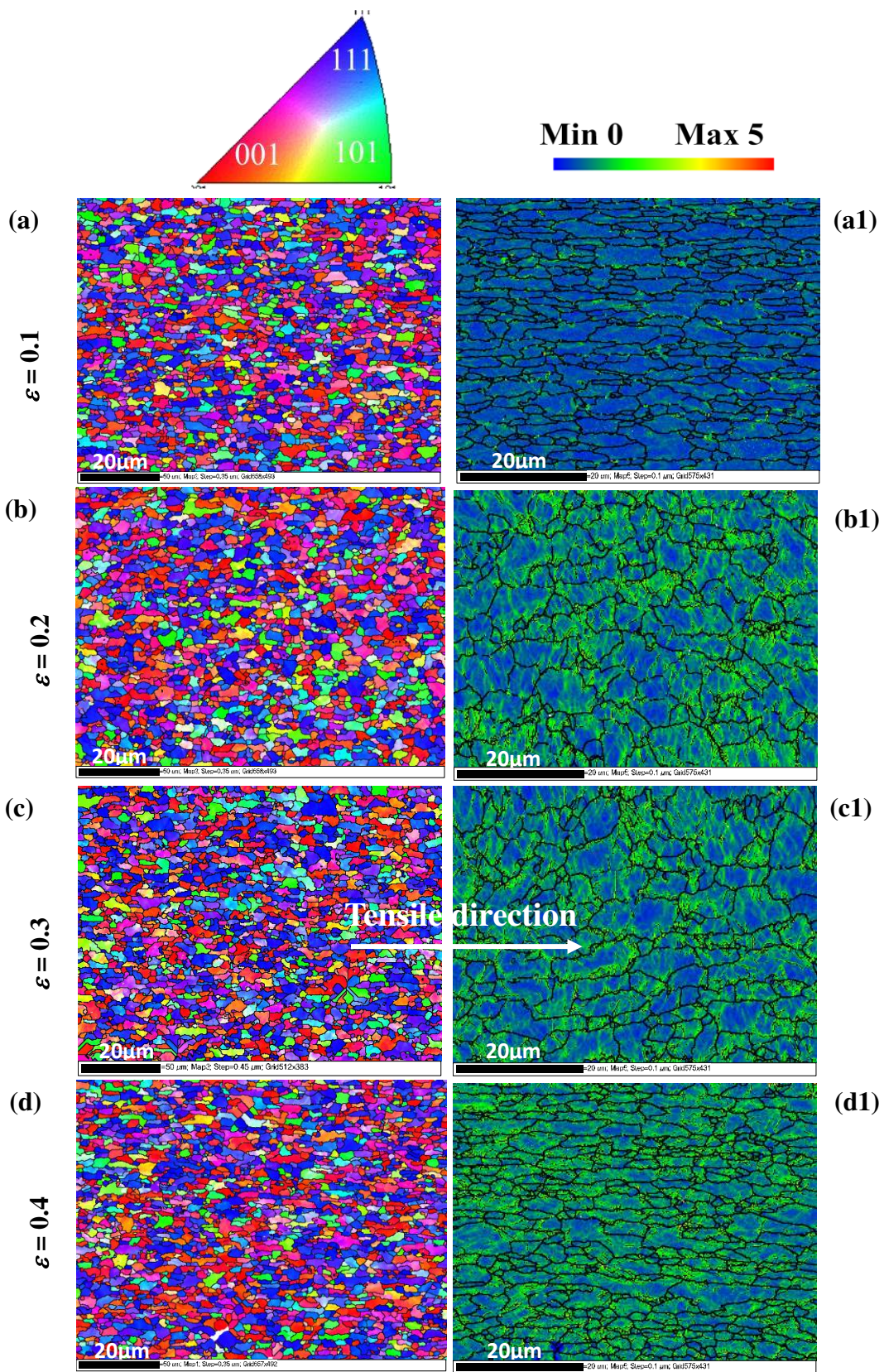


Fig. 8. (211) ferrite peaks for steels C, F, and H. Solid curves are the original experimental data. Two sub-peaks (short dash and dash dot curves) are derived from the solid curves, revealing the bainitic ferrite and ferrite. Steel C: 820°C/120s + 400°C/300s; F: 850°C/120s + 420°C/300s; H: 850°C/120s.



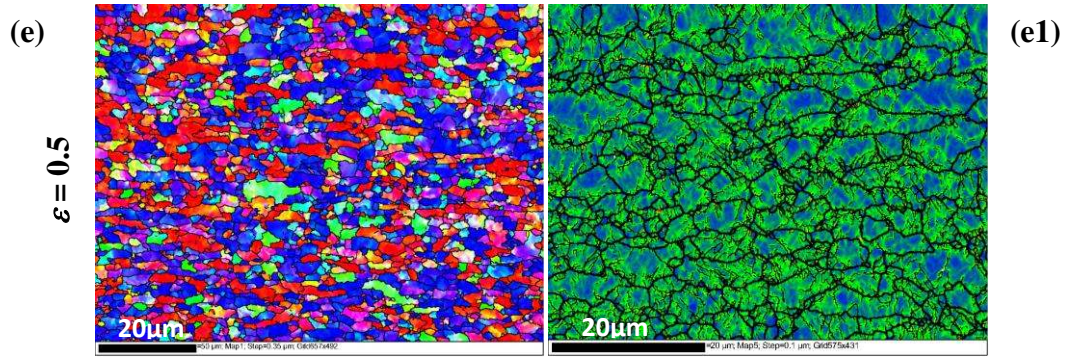


Fig. 9 (a) – (e) inverse pole figure (IPF) maps for steel C at different strain levels, with blue for $\langle 111 \rangle // \text{RD}$, red for $\langle 001 \rangle // \text{RD}$, and green for $\langle 101 \rangle // \text{RD}$, indicated by an inset at the right bottom of (a). (a1) – (e1) show the corresponding kernel average misorientation (KAM) maps with strain in steel C ($820^\circ\text{C}/120\text{s} + 400^\circ\text{C}/300\text{s}$).

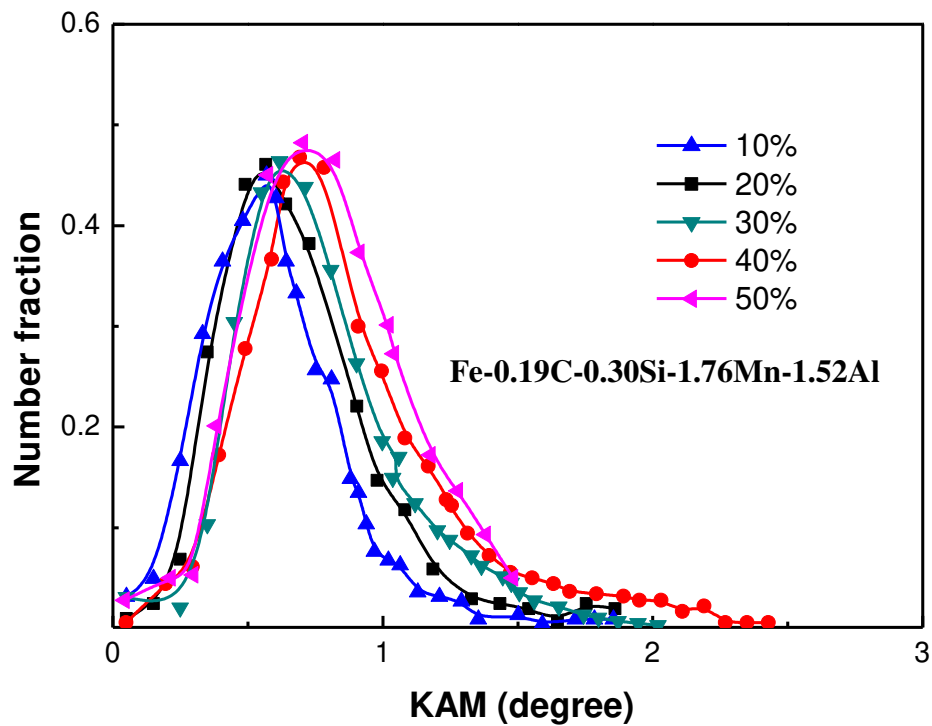


Fig. 10. Evolution of the kernel average misorientation (KAM) distribution of deformed steel C ($820^\circ\text{C}/120\text{s} + 400^\circ\text{C}/300\text{s}$) as a function of strain.

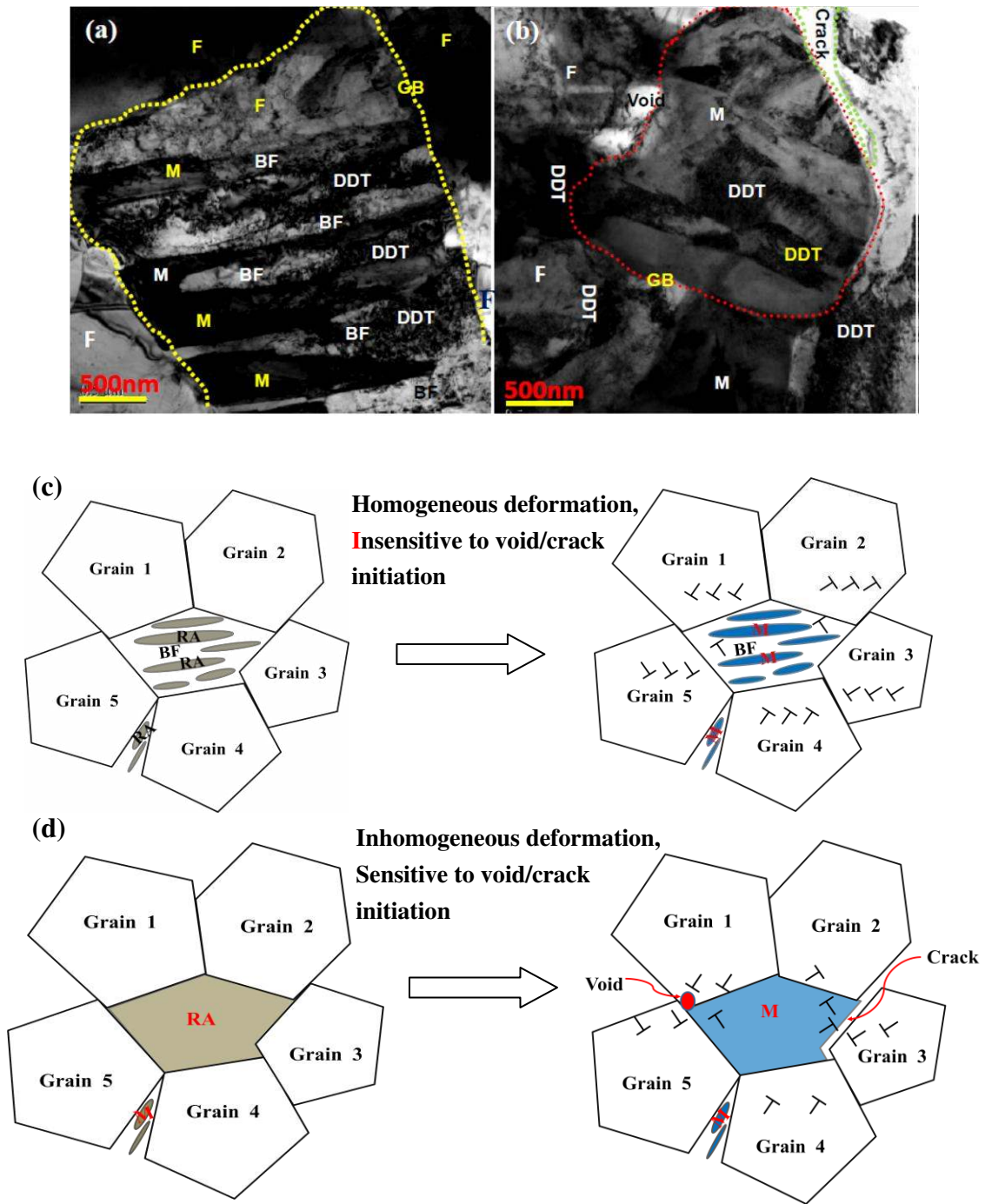


Fig. 11. TEM observations of the deformation microstructures in regions close to the fracture surface of steels C (a) and H (b), respectively. The schematic illustrations show the possible mechanism which is responsible for the failure of steels C (c) and H (d). F: ferrite, M: martensite, BF: bainitic ferrite, DDT: dense dislocation tangles, and GB: grain boundary. Steel C: 820°C/120s + 400°C/300s; steel F: 850°C/120s + 420°C/300s; steel H: 850°C/120s.

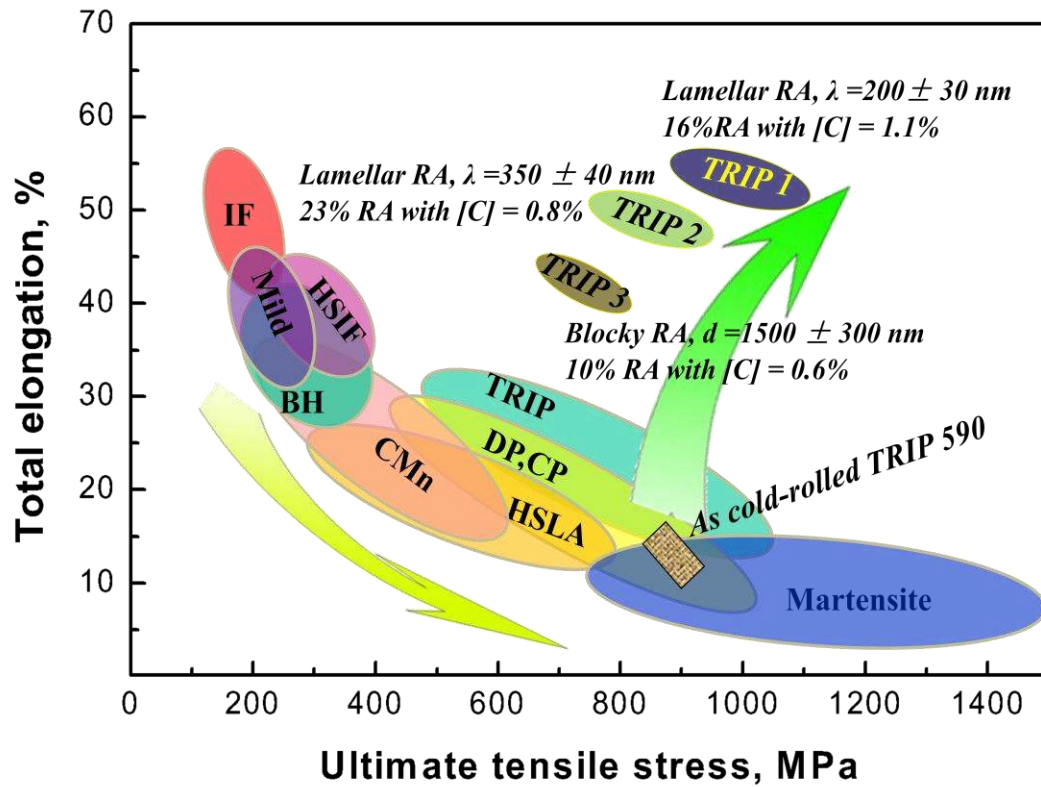


Fig. 12. Strategy for achieving a substantially-improved combination of ultrahigh strength and good ductility, compared to current steels used in automotive applications. TRIP 1 and TRIP 2 represent steels C and F, characterized by the lamellar RA with an average thickness of 200 nm and 350 nm, respectively; TRIP 3 represents steel H containing more blocky-shaped RA with an average size of 1,500 nm. IF: interstitial-free steel; HSIF: high-strength-interstitial-free steel; Mild: mild steel; BH: baked-hardening steel; CMn: C-Mn steel; TRIP: transformation-induced-plasticity steel; DP: duplex phases steel; CP: complex phases steel; HSLA: high-strength-low-alloy steel; Martensite: martensite steel.